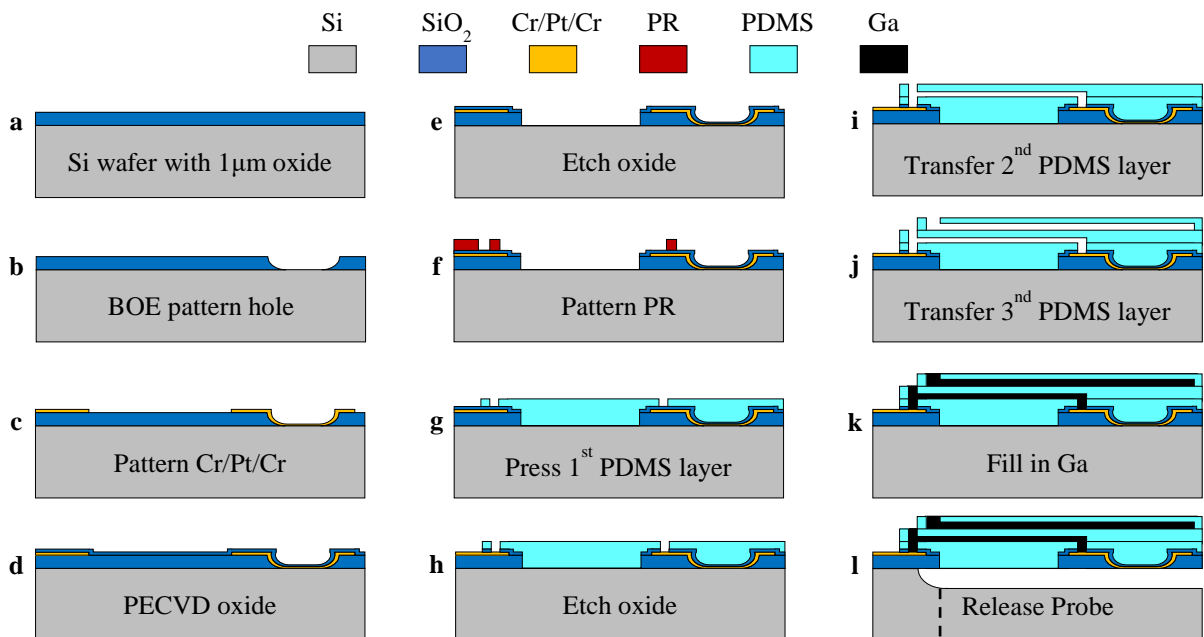


## Supplementary Figure S1



**Supplementary Fig. 1 | Fabrication of ULTS probes.**

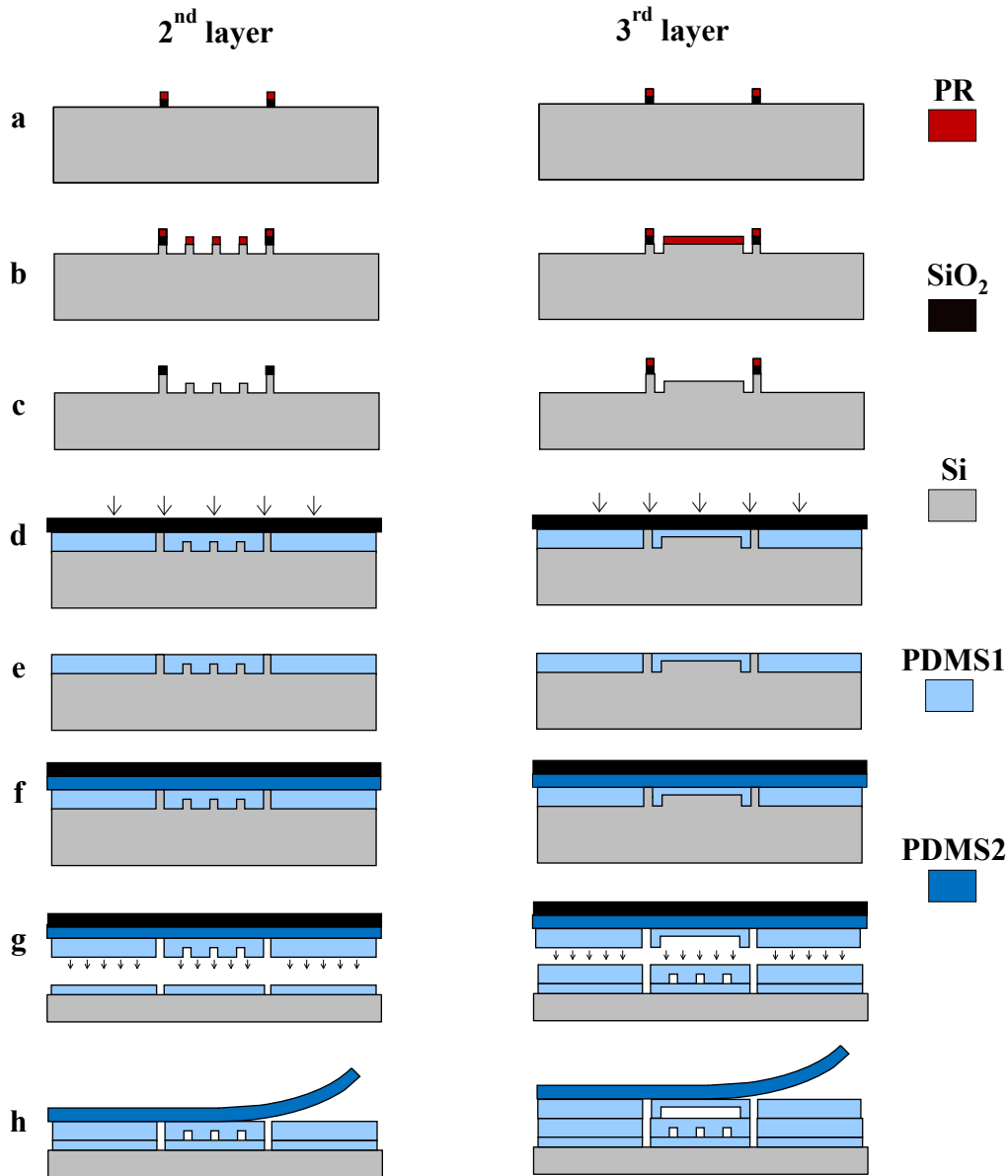
The multifunctional ULTS probes were fabricated using both conventional MEMS fabrication and a customized PDMS thin-film transfer process.

- a) A 1  $\mu\text{m}$  thick thermal oxide layer was grown on a Si wafer.
- b) Trenches at the probe tips were patterned by photolithography using photoresist AZ5214-IR (AZ Electronic Materials) and etched by buffered oxide etch (BOE) to expose the electrodes on the backside of the probes after the final release process.
- c) 20 nm/100 nm/20 nm Cr/Pt/Cr metal layers were deposited by an e-beam evaporator (CHA Industries) and patterned by a lift-off process to define electrodes and soldering pads.
- d) A 400 nm layer of  $\text{SiO}_2$  was deposited by PECVD (Surface Technology Systems) that serves as a bonding layer between metal and PDMS.
- e) The electrodes and soldering pads were isolated by removing the  $\text{SiO}_2$  layer in between using photolithography and RIE etching (Surface Technology Systems)
- f) A layer of  $\sim 5 \mu\text{m}$  thick photoresist AZ4620 was spun on the wafer at 6,000 rpm and patterned by photolithography to define the outlines of probes and vias.
- g) To connect the electrodes and soldering pads, poly(dimethylsiloxane) (PDMS; Sylgard 184, Dow Corning) was patterned using a “lift-off” process. PDMS was prepared by first mixing 10 g pre-polymer with 10  $\mu\text{L}$  Pt catalyst (Pt-divinyltetramethyldisiloxane complex; 2% Pt in xylene; Gelest, Inc) and then mixing with 1g of cross-linker. Pt catalyst was used to speed up the curing process at room temperature ( $\sim 6$  hours). Uncured PDMS was poured on the oxygen plasma treated wafer (500 mT, 80 W, 30 s; Technics Micro-RIE, Series 800), and pressed by an 1H,1H,2H,2H perfluorooctyltriethoxysilane (silane) (Sigma-Aldrich) treated glass to drive excess PDMS out of the mold. After curing, the glass was peeled off and a

PDMS thin-film was left on the wafer. The wafer was then sonicated in acetone to remove AZ4620.

- h) SiO<sub>2</sub> on top of the electrodes were exposed by RIE etching (Surface Technology Systems).
- i) The second layer of PDMS thin-film was transferred and bonded to the first PDMS thin-film that forms microchannels for liquid metal interconnects and drug deliveries (Supplementary Fig. 2).
- j) The third layer of PDMS thin-film was transferred and bonded to form a microchannel for temporary stiffening purpose (Supplementary Fig. S2).
- k) Liquid gallium (Ga) was filled into microchannels and frozen.
- l) ULTS were released by XeF<sub>2</sub> undercut, and cleaved to the desired length.

## Supplementary Figure S2



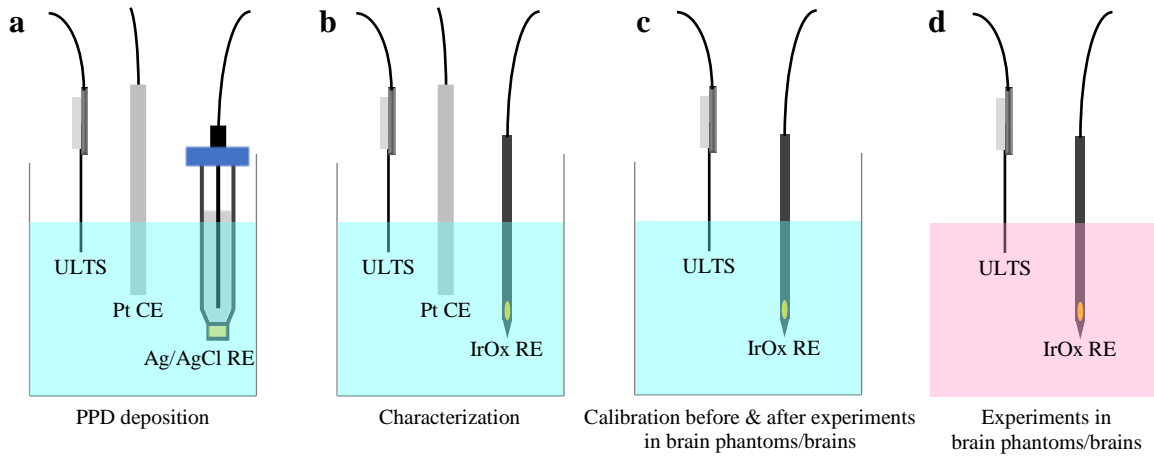
### Supplementary Fig. S2 | PDMS thin-film transfer process.

Si molds were fabricated on a 4-inch wafer with a layer of thermal oxide

- To define the spacer of the PDMS thin-film, the thermal oxide layer was patterned by photolithography and RIE etching. Photoresist was then stripped by oxygen plasma (Matrix 105, Spectrum).
- To define the microchannels, a second layer of photoresist was deposited and patterned. Deep reactive ion etching (DRIE, PlasmaTherm SLR 770 ICP) was used to etch Si to define the microchannel thickness. Photoresist was then stripped by oxygen plasma.

- c) Si was further etched by DRIE with thermal oxide as etching mask to define the total thickness of the molds.
- d) PDMS prepared as described before was poured into the mildly silane treated Si molds (3  $\mu\text{L}$ , deposited 6 hours) and pressed by heavily silane treated glass (20  $\mu\text{L}$ , deposited >24 hours) for ~6 hours at room temperature.
- e) The silane treated glass was peeled-off, leaving the PDMS thin-film inside the mold. Silane treatment can be used to decrease the adhesion force with the following PDMS layer (1  $\mu\text{L}$ , deposited 10 mins).
- f) Another layer of PDMS was poured on top of the thin-film and cured for ~6 hours at room temperature to create a PDMS buffer.
- g) The PDMS thin-film was peeled-off along with the PDMS buffer and bonded to the previous PDMS layer using a Quintel mask aligner.
- h) The PDMS buffer was peeled-off, leaving the PDMS thin-film bonded with the substrate.

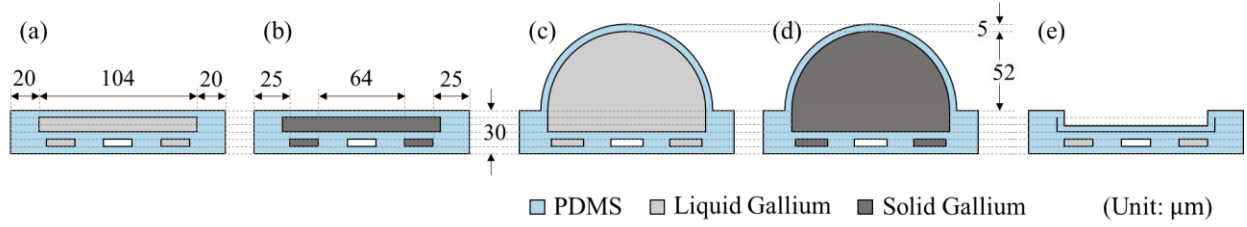
## Supplementary Figure S3



### Supplementary Fig. S3 | Setups for electrochemical experiments.

- Deposition of PPD on electrodes was conducted using a three-electrode system with Pt counter electrode (CE) and Ag/AgCl reference electrode (RE).
- Characterization of the sensitivity, selectivity and linear range was conducted using a three-electrode system with Pt CE and IrOx RE.
- Biosensors were calibrated for before and after experiments in brain phantoms/brains using a two-electrode system with IrOx RE.
- Sensing experiments in brain phantoms/brains were conducted using the same setup as the calibration step c).

## Supplementary Figure S4



### Supplementary Fig. S4 | Calculation of the bending stiffness for NUTS in different states

- “Soft” and “flat” state
- “Stiff” and “flat” state
- “Soft” and “inflated” state
- “Stiff” and “inflated” state
- “Soft” and “deflated” state

The bending stiffness per width  $D$  depended on its cross-section and the material properties, as

$$D = \sum_i \frac{E_i I_i}{w} \quad (1)$$

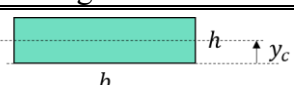
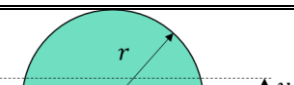
where  $w$  is the probe width ( $144 \mu\text{m}$ ),  $E$  is the Young's modulus of material ( $E_{\text{Liquid-Gallium}}$  is  $\sim 0 \text{ Pa}$ ,  $E_{\text{Forzen-Gallium}}$  is  $\sim 10 \text{ GPa}$ ,  $E_{\text{PDMS}}$  is  $\sim 1 \text{ MPa}$ ), and  $I$  is the second moment of area with respect to the neutral axis. It is easier to derive the second moment of area with respect to its central axis, and use the parallel axis theorem to derive the second moment of area with respect to the neutral axis, as

$$I = \sum_j \left[ I_{cj} + A_j (y_{cj} - \bar{y})^2 \right] \quad (2)$$

where  $A$  is the area of the shape,  $I_c$  is the second moment of area with respect to its central axis,  $y_c$  is the location of its central axis, and  $\bar{y}$  is the location of neutral axis. The expression to calculate  $A$ ,  $I_c$  and  $y_c$  are summarized in the **Table 1**. The location of neutral axis  $\bar{y}$  can be written as





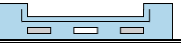
$$\bar{y} = \frac{\sum_j E_j A_j y_{cj}}{\sum_j E_j A_j} \quad (3)$$

**Table 1.** The area, second moment of area and the central axis location of rectangle and semicircle

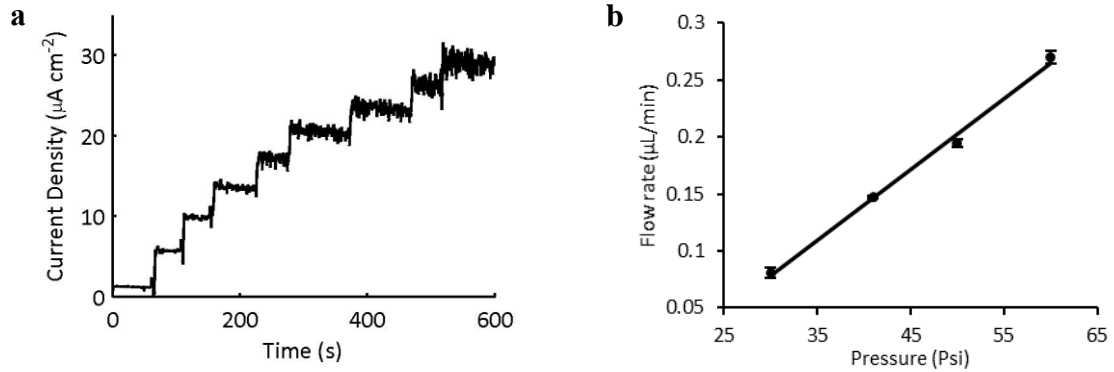
Rectangle	$I_c$	$A$	$y_c$	Semicircle	$I_c$	$A$	$y_c$
	$\frac{bh^3}{12}$	$bh$	$\frac{h}{2}$		$\frac{r^4(9\pi^2 - 64)}{72\pi}$	$\frac{\pi r^2}{2}$	$\frac{4r}{3\pi}$

The calculation results of five models are shown in **Table 2**, where the inflated shape with solid gallium has the highest bending stiffness per width ( $1.41 \times 10^{-4} \text{ N}\cdot\text{m}$ ) for tissue penetration and the deflated shape with liquid gallium has the lowest bending stiffness per width ( $1.32 \times 10^{-9} \text{ N}\cdot\text{m}$ ) to reduce micromotion-induced damage. Therefore, the range of tunable stiffness can be as large as  $10^5$ , where the gallium phase change contributes close to 4 orders of magnitude difference (“stiff” and “inflated” vs. “soft” and “inflated”), while the shape change contributes to the remaining 10-fold difference (“soft” and “inflated” vs. “soft” and “deflated”).

**Table 2.** The location of neutral axis and the bending stiffness per width of models

					
$\bar{y} (\mu\text{m})$	13.85	18.42	24.60	43.20	12.56
$D (\text{N}\cdot\text{m})$	$1.89 \times 10^{-9}$	$2.05 \times 10^{-6}$	$1.56 \times 10^{-8}$	$1.41 \times 10^{-4}$	$1.32 \times 10^{-9}$

## Supplementary Figure S5

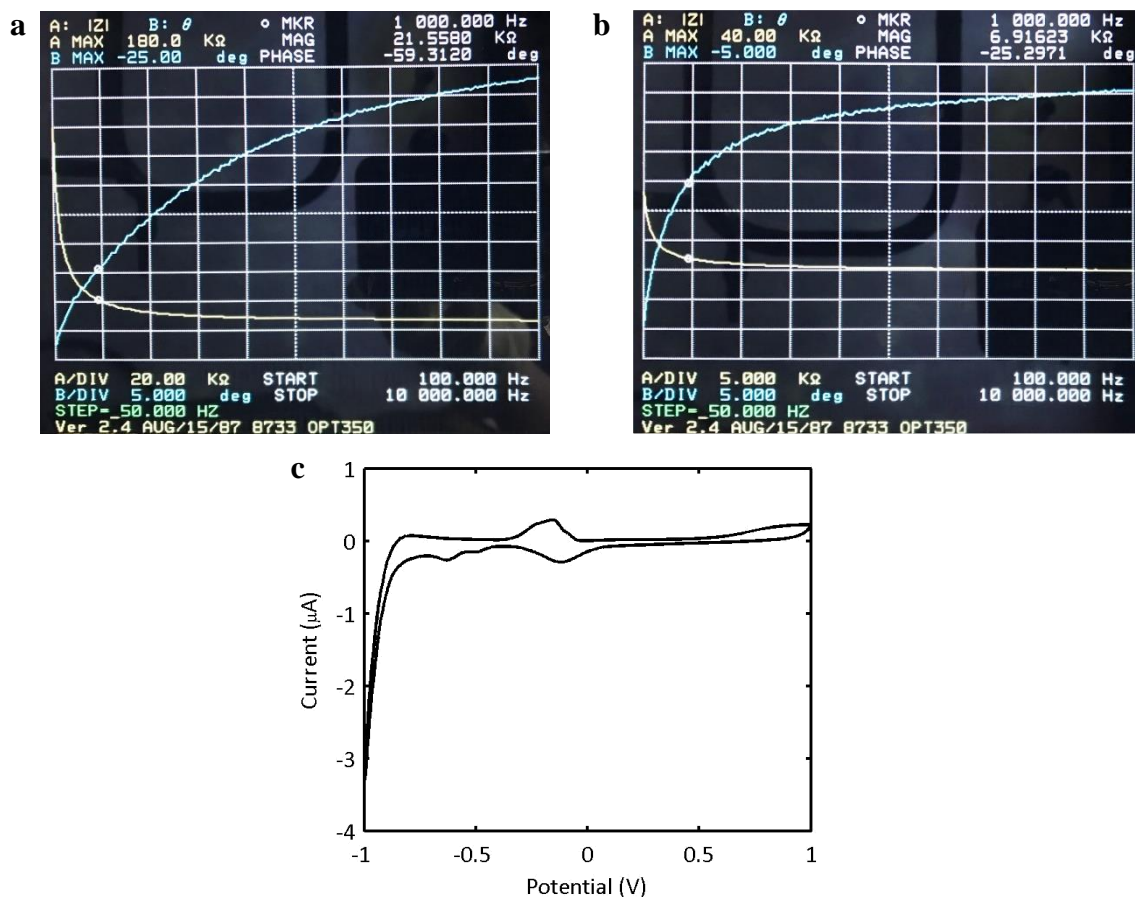


### Supplementary Fig. S5 | Characterization of the electrochemical sensor and liquid channel

- A representative current response of the biosensor to Glut. The biosensor response in a stirred PBS buffer (pH 7.4) was recorded for sequential injection of Glut to given concentrations of 20, 40, 60, 80, 100, 120, 140 and 160  $\mu\text{M}$  at a constant potential of 0.6 V (vs. IrOx).
- Flow rate of the microfluidic channel at different pumping pressures shows a linear relationship versus pumping pressure ( $R^2 = 0.995$ ) and high repeatability ( $n = 3$ ).



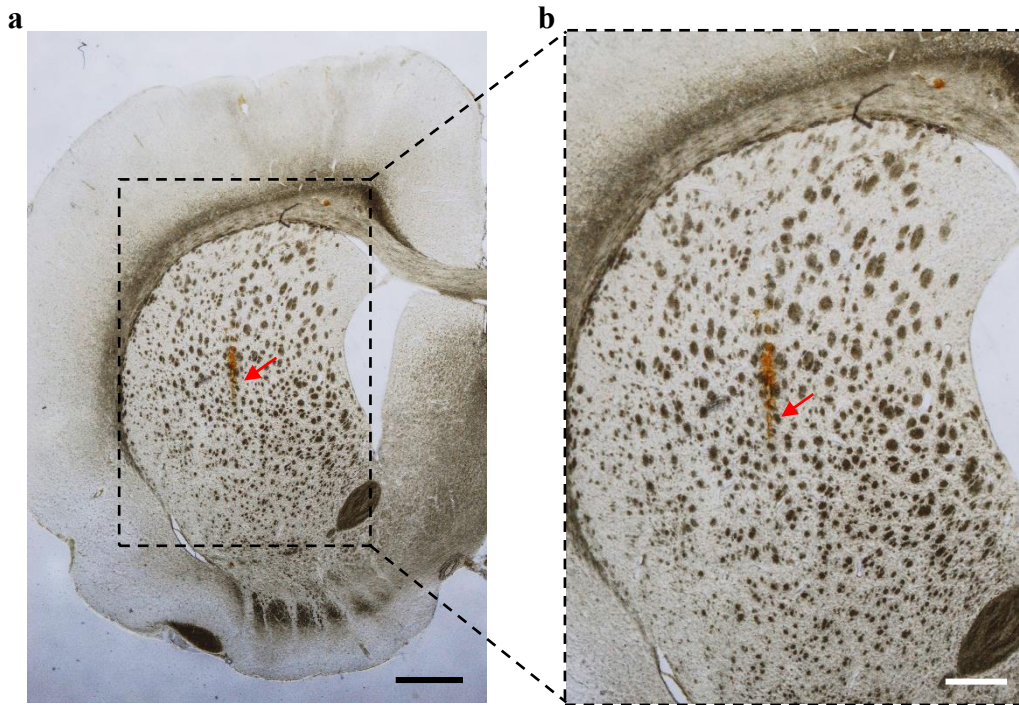
## Supplementary Figure S6



### Supplementary Figure S6 | Electrical characterization of electrodes.

- A representative electrochemical impedance spectroscopy (EIS) measurement of a regular Pt electrode of the ULTS probe in saline solution (pH 7.4). The impedance of the regular electrodes,  $21.4 \pm 1.50 \text{ k}\Omega$  ( $n = 5$ ) at 1 kHz, is similar to the Pt electrodes on Si probes.
- The impedance decreases to  $6.74 \pm 0.49 \text{ k}\Omega$  ( $n = 3$ ) at 1 kHz with the electrodeposition of rough Pt grass surface.
- Cyclic Voltammetry (CV) measurement of the Pt grass coated electrodes in saline (pH 7.4) in the range of -1 V to 1 V vs. Ag/AgCl, with a potential scan rate of 100 mV/s. Charge storage capacity is determined by the *integral area of CV curve* / ( $2 \times \text{scan rate}$ ) / surface area =  $2.54 \mu\text{C} / 5656 \mu\text{m}^2 = 4.5 \text{ mC}/\text{cm}^2$ .

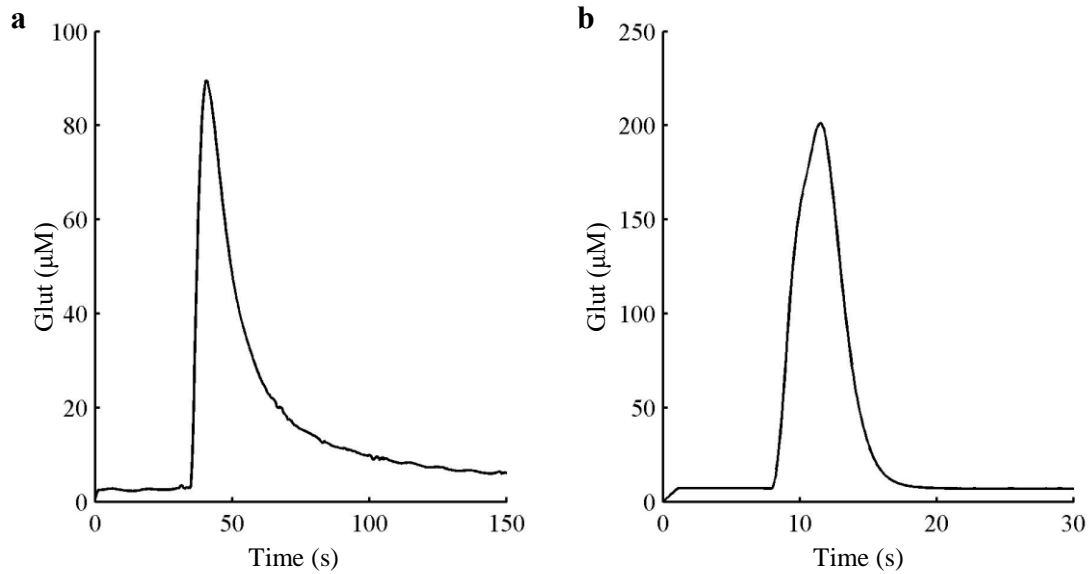
## Supplementary Figure S7



### Supplementary Fig. S7 | Probe insertion into the rat striatum

- a) Bright field image of a brain slice cut along the probe insertion direction. The red arrow indicates the implanted position of the probe in the rat striatum, evidenced by the wound caused by the acute implantation process. Scale bar: 1 mm
- b) Zoomed-in view of the brain slice. Scale bar: 0.5 mm

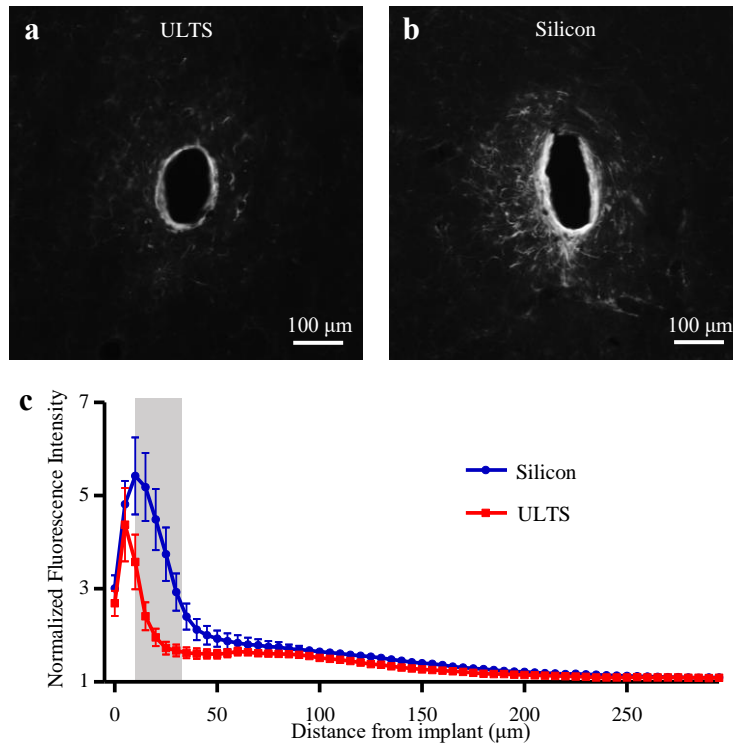
## Supplementary Figure S8



### Supplementary Fig. S8 | Comparison of glutamate ejection and detection in gel and *in vivo*

- Glut (150  $\mu\text{M}$ ) injection (60 psi, 2.4 s) in the brain phantom with a slow signal decay ( $\sim 100$  s) by pure diffusion.
- Glut (500  $\mu\text{M}$ ) injection (60 psi, 2.4 s) in the rat striatum with a fast signal decay ( $\sim 5$  s) representing the active reuptake in brain tissue.

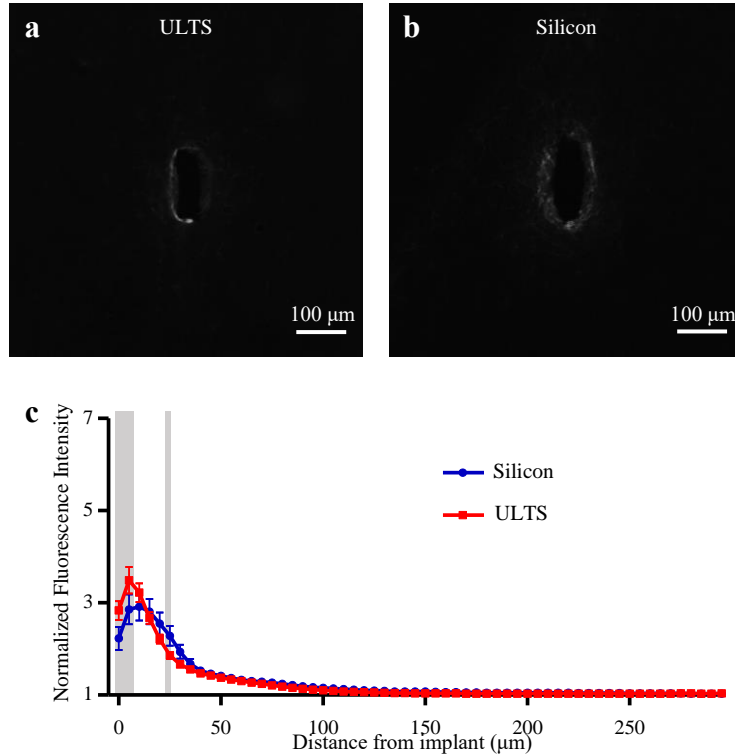
## Supplementary Figure S9



### Supplementary Fig. S9 | Immunohistochemical analysis of the astrocytic scar around the implantation site of a ULTS probe and a size-matched Si probe implanted in the same animal 4 weeks post-implantation.

- Representative fluorescence microscopy image of GFAP expression around a ULTS probe in horizontal section.
- Representative fluorescence microscopy image of GFAP expression around a silicon probe in horizontal section.
- Fewer astrocytes surround the ULTS probe compared to the silicon probe. Fluorescence intensity of GFAP expression from the implant-tissue interface to 300 μm away, with 5 μm bin size distance, normalized to the intensity at 500-550 μm (ULTS:  $n = 10$  sections, Silicon:  $n = 10$  sections. Two-way ANOVA, probe type  $\times$  distance interaction:  $F_{(59,1080)} = 4.95$ ,  $p < 0.0001$ ; Bonferroni post-test for distance at 10-30 μm:  $p < 0.0001$ , distance at 30-35 μm:  $p < 0.001$ ). Gray shadow denotes the area of significant difference between the ULTS and Silicon probes. Error bars represent SEM.

## Supplementary Figure S10



**Supplementary Fig. S9 | Immunohistochemical analysis of the astrocytic scar around the implantation site of a ULTS probe and a size-matched Si probe implanted in the same animal 9 weeks post-implantation.**

- Representative fluorescence microscopy image of GFAP expression around the ULTS probe in horizontal section.
- Representative fluorescence microscopy image of GFAP expression around the silicon probe in horizontal section.
- Thinner scar encapsulation around ULTS than silicon probes 9 weeks after implantation, despite the higher GFAP expression at the surface of ULTS which is possibly due to the hydrophobic nature of PDMS. (ULTS:  $n = 21$  sections, Silicon:  $n = 16$  sections. Two-way ANOVA, probe type  $\times$  distance interaction:  $F_{(59,2100)} = 1.98$ ,  $p < 0.0001$ ; Bonferroni post-test for distance at 0-10  $\mu\text{m}$ :  $p < 0.0001$ , distance at 25-30  $\mu\text{m}$ :  $p < 0.01$ ). Gray shadow denotes the area of significant difference between the ULTS and Silicon probes. Error bars represent SEM.

## Supplementary methods

### 1. Calibration of flow rate

ULTS probes were connected to microfluidic tubing with a known volume of preloaded liquid, connected to a constant pressure source. Probes were then implanted into a brain phantom to simulate the brain environment. The time required for ejecting all the preloaded liquid in the tubing was recorded to determine the flow rate. Flow rates at different pumping pressures (30-60 psi) were measured for 3 times to determine the system reproducibility.

### 2. Chronic implantations

Male Sprague Dawley rats (270-300 g) were anaesthetized with isoflurane, administered carprofen (5 mg/kg s.c., Rimasyl, Zoetis) and placed in a standard stereotaxic frame. Implantation procedures were as described above with the addition of placement of a second, Si-wafer-based, probe with similar dimensions (thickness: ~35  $\mu\text{m}$ , width: tapered from 200 to 144  $\mu\text{m}$ ) into the contralateral striatum. The implants were anchored by 4 bone screws and affixed with dental cement. Rats received an additional dose of carprofen (5 mg/kg) 24 h later for pain management, and sulfamethoxazole and trimethoprim oral suspension (0.5% in water, Hi-Tech Pharmacal Co., INC, Amityville, NY 11701) for 10 days to prevent infection.

### 3. Immunohistochemistry

Rats, chronically implanted with ULTS and silicon probes, were terminally anesthetized with pentobarbital (100 mg/kg, i.p) and transcardially perfused with heparinized phosphate-buffered saline (PBS, 2 mg heparin/100 mL) followed by ice-cold 4% paraformaldehyde in PBS prior to

decapitation. Probes were carefully withdrawn, and brains were removed and postfixed for ~12 h at 4 °C with 4% paraformaldehyde in PBS after which the 4% paraformaldehyde solution was replaced by 30% sucrose in PBS at 4 °C. After 2 days, 40 µm horizontal sections in through the region of probe placement were collected for immunostaining using a LEICA CM 1950 cryosectioning instrument. Sections were washed three times in PBS (10min each) and blocked using a solution consisting of 0.1% Triton and 5% donkey serum in PBS for 2 h at room temperature. Slices were then incubated with primary antibody (rabbit anti-GFAP 1:1000 dilution; Millipore) containing 0.1% Triton and 5% donkey serum overnight at 4 °C. After incubation, slices were rinsed 3 times in 3× PBS (10min/each) and 1 time with 1× PBS (10min/each) before incubation for 2 h at room temperature with secondary antibody (Alexa Fluor 488 donkey anti-rabbit 1:100 dilution; Invitrogen) diluted with 2% donkey serum/0.1% Tween in 1x PBS. Slices were then washed 3 times with 0.1% Tween in 1× PBS (10min/each) and 1 time with 1× PBS (10min/each) before mounting on glass slides with coverslips using Aqua-Mount (Richard-Allan Scientific). The slides remained in the dark at 4 °C before microscopic imaging.

#### 4. Imaging and Image Data Analysis

Fluorescence images of brain sections were acquired on an Axio Scope A1 microscope (Zeiss) with an AxioCam MRm camera (Zeiss). Exposure time and other imaging parameters were held constant for all samples. Representative fluorescence images were slightly enhanced using ImageJ to improve visual display, while all the analysis was based on raw images.

Following image acquisition, pixel-based image intensity analysis was performed using a modified MATLAB program based on a published custom MATLAB script

I.N.T.E.N.S.I.T.Y.(Du et al., 2017). In short, an ellipse was drawn to locate the implant-tissue interface. The fluorescence intensity was quantified in 5  $\mu\text{m}$  bins of expanding concentric ellipses around the implantation site up to 300  $\mu\text{m}$  and normalized against the baseline intensity, which was defined as the average intensity in the interval of 500-550  $\mu\text{m}$  away from the center of the implantation site. Statistical analysis was performed using Prism 5.0 (GraphPad Software, USA).

#### Supplementary reference

Du, Z.J., Kolarcik, C.L., Kozai, T.D.Y., Luebben, S.D., Sapp, S.A., Zheng, X.S., Nabity, J.A., Cui, X.T., 2017. Ultrasoft microwire neural electrodes improve chronic tissue integration. *Acta Biomaterialia* 53, 46–58. <https://doi.org/10.1016/j.actbio.2017.02.010>